PAPER

Check for updates

Enhanced ionic conductivity in electroceramics by nanoscale enrichment of grain boundaries with high solute concentration†

William J. Bowman,*‡[a] Madeleine N. Kelly,[b] Gregory S. Rohrer,[b] Cruz A. Hernandez[a] and Peter A. Crozier ID *[a]

The enhancement of oxygen ionic conductivity by over two orders of magnitude in an electroceramic oxide is explicitly shown to result from nanoscale enrichment of a grain boundary layer or complexion with high solute concentration. A series of $Ca_xCe_{1-x}O_{2-\delta}$ polycrystalline oxides with fluorite structure and varying nominal Ca^{2+} solute concentration elucidates how local grain boundary composition, rather than structural grain boundary character, primarily regulates ionic conductivity. A correlation between high grain boundary solute concentration above ~40 mol%, and four orders of magnitude increase in grain boundary conductivity is explicitly shown. A correlated experimental approach provides unique insights into fundamental grain boundary science, and highlights how novel aspects of nanoscale grain boundary design may be employed to control ion transport properties in electroceramics.

Electroceramics serve as solid electrolytes and electrodes for wide-ranging applications in energy storage,[1] energy conversion,[1] gas separation,[2] gas sensing,[3] and information[4] technologies. High ionic conductivity, which is often desired to optimize device performance, is degraded by grain boundaries (GBs) with nanometer dimensions that act as ionic blocking layers in polycrystalline electrolytes.[5–11] For example, GB ionic conductivity (σ_{GB}) can be 10^2–10^6 times lower than grain conductivity in common oxygen-conducting solid solutions based on ceria (CeO_2) or zirconia (ZrO_2), *e.g.* $Gd_xCe_{1-x}O_{2-\delta}$ and $Y_xZr_{1-x}O_{2-\delta}$;[5–8,11] with similar effects occurring in solid lithium ion conductors for all-solid-state batteries[10] and proton conductors.[3,9] Moreover, nanoscale compositional and chemical phenomena that influence the electrical properties of oxide GBs—such as highly localized deviation from bulk stoichiometry, and/or charge carrier accumulation/depletion—may also be relevant for understanding oxide thin films and hetero-interfaces, which are widely implemented throughout fundamental materials research and device development.[4,12–14]

Early studies of GB conductivity in ceria and zirconia showed that highly resistive intergranular amorphous phases could form due to segregation of impurities present in chemical precursors of relatively low purity.[5] However, even in high-purity polycrystalline materials, high GB resistivity persists (*e.g.* ref. 8 and 11), and is now widely attributed to electrostatic GB space charge effects. As GB effects impact the electrical transport properties of many polycrystalline systems, it is thus important to elucidate how nanoscale and atomic-level composition and structure regulate ionic conductivity. This fundamental understanding will guide fabrication of GBs with optimized transport properties for different applications. In solid ionic conductors, it is common to add aliovalent solute cations to increase the concentration of charge-compensating vacancies, which act as mobile charge carriers to enhance ionic conductivity. For GBs in polycrystalline oxides of high purity, measurements show that σ_{GB} can increase by several orders of magnitude with nominal aliovalent solute concentration.[8,15] The crystallographic character of the GB can also cause significant changes in GB conductivity, and conductivity measurements of oxide bicrystals of fixed nominal solute concentration showed that σ_{GB} can vary by up to a factor of 10 with changes in the relative crystal orientation and GB plane, *i.e.* the *structural grain boundary character*.[16]

Efforts to maximize σ_{GB} have focused in part on altering the intrinsic GB electrostatic double layer space charge potential that influences the distribution of charge carriers within nanometers of the GB, and contributes to hindering ionic migration by reducing the carrier concentration. However, there are some

[a]School for Engineering of Matter, Transport and Energy, Arizona State University, 501 E. Tyler Mall, Tempe, Arizona 85287-6106, USA. E-mail: wjbowman@mit.edu, crozier@asu.edu

[b]Department of Materials Science and Engineering, Carnegie Mellon University, 5000 Forbes Avenue, Pittsburgh, Pennsylvania 15213, USA

†Electronic supplementary information (ESI) available: Sample fabrication, grain boundary characterization, and EELS quantification. See DOI: 10.1039/c7nr06941c

‡Present Addresses: Laboratory for Electrochemical Interfaces, Massachusetts Institute of Technology, 77 Massachusetts Ave., Cambridge, MA, 02139, USA.

contradictory results in the literature regarding the influence of GB solute accumulation on σ_{GB}. Shirpour et al.[9] combined electrochemical and TEM-based spectroscopic measurements to demonstrate that segregation of Y^{3+} and Sc^{3+} solutes to GBs in proton-conducting perovskites $BaY_{0.06}Zr_{0.94}O_{3-\delta}$ and $BaSc_{0.06}Zr_{0.94}O_{3-\delta}$ resulted in an increase in the proton conductivity. Diercks et al.[17] used atom probe tomography to demonstrate that GBs in $Nd_{0.3}Ce_{0.7}O_{2-\delta}$ had both greater GB Nd^{3+} content and σ_{GB} when compared to $Nd_{0.1}Ce_{0.9}O_{2-\delta}$. Additionally, Avila-Paredes et al.,[18] Litzelman et al.,[14] and Mills et al.[13] employed electrochemical measurements to show that decoration of GBs with transition metal (TM) ions in $Gd_xCe_{1-x}O_{2-\delta}$ and $Y_xZr_{1-x}O_{2-\delta}$, so-called heterogeneous GB doping, could be used to reduce the magnitude of net positive charge of the GB potential barrier. (No local spectroscopic evidence directly confirming GB enrichment by TM ions was presented in those studies.) These works all pointed to the fact that di- and tri-valent solute ions, when substituted for the tetravalent host cation (i.e. Zr^{4+}, Ce^{4+}), serve to reduce the net positive potential of the GB core. However, Lin et al.[19] demonstrated experimentally that suppressing Gd^{3+} segregation to $Gd_{0.2}Ce_{0.8}O_{2-\delta}$ GBs could enhance σ_{GB} as well, which appears to be in direct contradiction to, e.g. Shirpour[9] and Diercks,[17] with respect to the effect of solute segregation on space-charge dominated σ_{GB}.

To interpret GB conductivity observations, researchers have successfully employed thermodynamic interface models such as Mott–Schottky and Gouy–Chapman models.[5,8,18,20–22] Although they have been successful in providing a framework to interpret the influence of space charge effects on σ_{GB}, the Mott–Schottky and Gouy–Chapman models are built on the so-called "dilute-solution" assumption. There is a growing body of experimental evidence[9,11,17,19,23–27] and theoretical predictions[26,28,29] which indicates the existence of solute cations at electroceramic GBs at concentrations significantly higher than the range of validity for the dilute solution assumption. These observations are not surprising considering the high temperatures and times typically employed for ceramic densification and the thermodynamic driving force to reduce the overall system energy via solute segregation. (It is worth noting too that modern high-speed sintering methods are also vulnerable to GB solute segregation.[9,27]) Solute segregation to GBs can be driven by cation size mismatch, electrostatic forces (i.e. GB core charge neutralization) and/or reduction in the GB energy.[9,23,27,29] This has motivated the recent development of a novel thermodynamic model[29] which treats GBs as interfaces in a concentrated solid solution, and thus considers cation/anion redistribution and defect–defect interactions.

At present, there are no direct experimental observations showing how high GB solute concentration affects σ_{GB} in oxide ion conductors. Here we use nanospectroscopy and electrical measurements to show that nanoscale GB solute concentrations greater than 40 mol% arise during conventional ceramic densification treatments and are correlated with a four-order-of-magnitude increase in σ_{GB}. Furthermore, it is shown that the large increase in σ_{GB} cannot be explained by

changes in GB character and must be a direct result of the high solute concentrations present at the GBs. We hypothesize that when strong dopant segregation takes place, σ_{GB} is primarily controlled by local nanoscale composition rather than GB character. The observations cannot be interpreted using the traditional low-solute concentration models, and point to the importance of developing new models which can be employed to describe σ_{GB} in the presence of high GB solute concentration.

A ceria solid solution containing divalent Ca^{2+} was selected as a model system to explore the role of GB character and composition on oxygen ionic conductivity. σ_{GB} was measured as a function of the nominal Ca^{2+} concentration (i.e. x in $Ca_xCe_{1-x}O_{2-x}$) using AC impedance spectroscopy. To differentiate the effects of GB structural character and composition, GB character distributions were measured using electron backscatter diffraction (EBSD) in a scanning electron microscope, and electron energy-loss spectroscopy (EELS) in an aberration-corrected scanning transmission electron microscope (AC-STEM) was used for atomic-resolution imaging and spatially resolved elemental analysis. This correlated experimental approach provided unique and novel insights into fundamental GB science and highlights aspects of GB design that are applicable to other polycrystalline electrolytes.

Dense polycrystalline pellets (e.g. Fig. 1f) were fabricated from spray-dried nanoparticles with composition $Ca_xCe_{1-x}O_{2-x}$ for three compositions corresponding to $x = 0.02$, 0.05 and 0.1 denoted 2CCO, 5CCO and 10CCO, respectively. Densification was performed by sintering the pellets in air at 1400 °C for 24 h. X-ray diffraction (XRD, $\lambda = 0.1541$ nm) patterns acquired from precursor nanoparticles and pellets showed no peaks from CaO_x phases, confirming the phase purity of the fluorite CCO (space group $Fm\bar{3}m$; see Fig. 1a and b). Grain conductivity (σ_{Grain}) and σ_{GB} were measured in the pellets using AC impedance spectroscopy, a volume-averaged technique that differentiates the unique impedance responses of grains and GBs, enabling measurement of the resistivity of each.[3,8,11] Representative impedance data from 10CCO are presented in Fig. 1c and d, as so-called Nyquist plots: imaginary vs. real impedance components parameterized by frequency. To extract grain and GB resistance (R_{Grain} and R_{GB}, respectively), Nyquist plots were fit with an equivalent circuit model (Fig. 1d inset) comprising a series combination of parallel resistor–capacitor subcircuits, each corresponding to the responses of the grain, GB and electrode. (Capacitors were approximated using constant phase elements, Q, which model non-ideal capacitors.[3]) With increasing temperature, the impedance response collapses towards the origin, indicating a decrease in R_{Grain} and R_{GB}—expected of a thermally activated ionic transport mechanism. From knowledge of pellet thickness, t, and electrode area, A, σ_{Grain} was calculated as

$$\sigma_{Grain} = \frac{1}{R_{Grain}}\frac{t}{A}. \tag{1}$$

Similarly, σ_{GB} was determined from R_{GB} using eqn (2), which accounts for differences in grain size, D_{Grain}, between
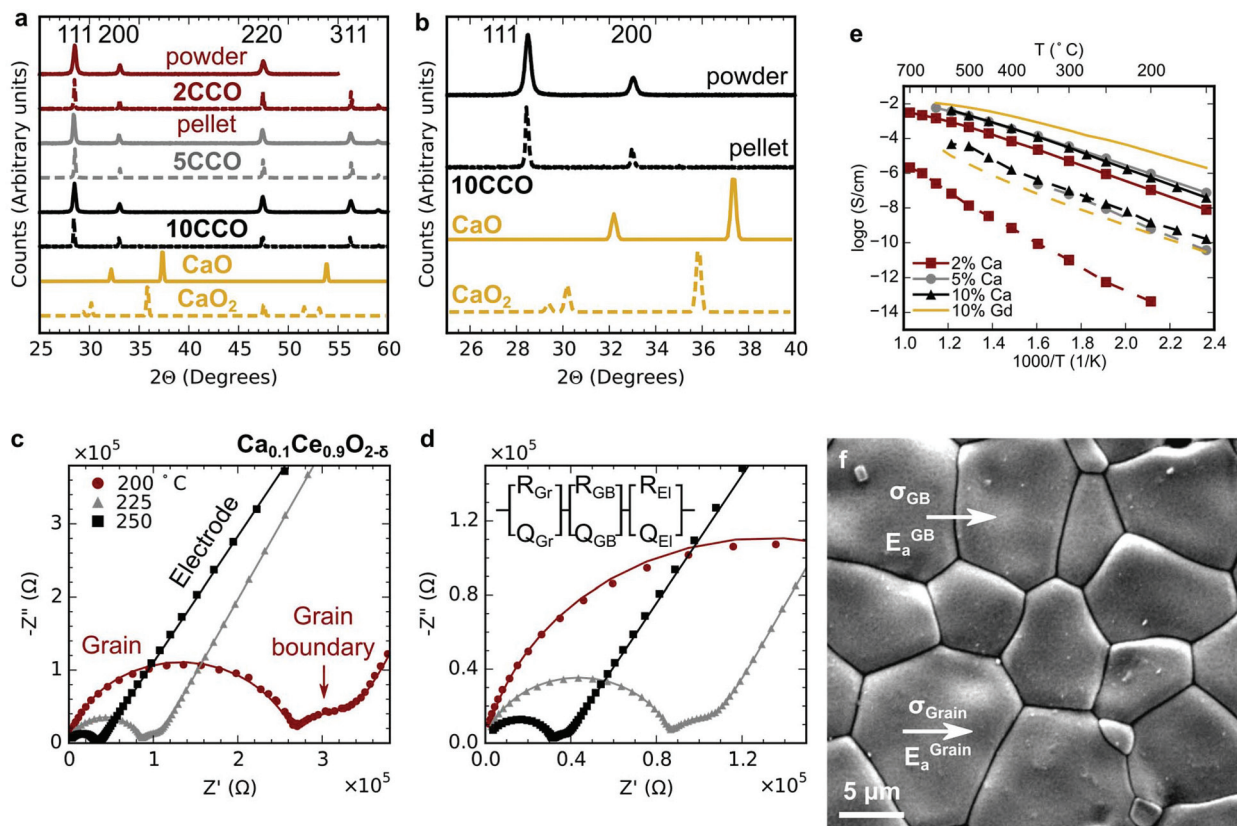
Fig. 1 (a) XRD patterns from CCO starting powders (solid curves) and pellets (dashed curves). CaO_x peaks are absent from CCO patterns; reference patterns for CaO[50] and CaO_2[51] are provided for comparison. (b) Expanded view of 10CCO and CaO_x reference spectra in (a). (c) Typical 10CCO Nyquist plots acquired at various temperatures; arcs correspond to the grain (Gr in the inset of (d)), grain boundary (GB) and electrode (El). Solid lines show fits to the equivalent circuit model inset in the expanded view (d). (e) Arrhenius plots of σ_{Grain} (solid curves) and σ_{GB} (dashed) of all CCO samples and 10GCO. (f) Secondary electron SEM image of the 2CCO pellet surface following sintering. Labelled arrows indicate grain and GB transport pathways through the pellet.

CCO pellets (measured from SEM images). This correction, which addresses differences in GB volume density, relies on knowledge of the boundary width, d_{GB}, taken to be the compositional GB width measured using EELS (see below). Eqn (2) arises from the brick-layer model for dense polycrystalline conductors, which approximates grains as packed cubes separated by a GB layer; model derivation and discussion are given elsewhere.[3] In the context of the brick-layer model, because $\sigma_{Grain} \gg \sigma_{GB}$, we assume negligible ion migration along boundaries parallel to the conduction direction. Thus σ_{GB} here refers only to ionic migration across boundaries perpendicular to the conduction direction.

$$\sigma_{GB} = \frac{1}{R_{GB}} \frac{t}{A} \frac{d_{GB}}{D_{Grain}}. \quad (2)$$

For the materials investigated here, conductivities are assumed to be ionic, as electronic conduction in CCO is negligible at the solute concentrations, temperatures and oxygen partial pressures employed.[30] Fig. 1e presents σ_{Grain} and σ_{GB} measured in all CCO samples, and for comparison, $Gd_{0.1}Ce_{0.9}O_{1.95-\delta}$ (10GCO)—a widely-employed fast oxygen ion conductor (notice that σ_{Grain} of 10GCO exceeds that of CCO).

A marked difference between σ_{Grain} and σ_{GB} for each composition is apparent, with σ_{Grain} typically exceeding σ_{GB} by 10^4–10^7 times depending on the nominal Ca^{2+} concentration and temperature. When comparing the total conductivity of these materials, which comprises the grain and GB, 2CCO was 2–4 orders of magnitude lower than 5CCO and 10CCO (see Fig. S2†). Noteworthy, is the pronounced difference (a factor of 10^3–10^4) between σ_{GB} of 2CCO and that of 5CCO and 10CCO. Furthermore, σ_{GB} in 5CCO and 10CCO is comparable to 10GCO, suggesting that Ca^{2+} may be a promising candidate for heterogeneous GB doping schemes aimed at optimizing σ_{GB}.

Table 1 shows grain and GB migration activation energies (E_a^{Grain} and E_a^{GB}, respectively) determined from slopes of $\ln(\sigma T)$ vs. $1/T$ using

$$\sigma T = \sigma_0 e^{\frac{-E_a}{kT}} \quad (3)$$

where σ_0 is the conductivity pre-exponential and E_a represents the effective migration activation energy. E_a^{Grain} was determined below 450 °C because at higher temperatures there is an oxygen vacancy order-to-disorder transition which liberates mobile vacancies, lowering the effective migration activation

Table 1 Microstructure, electrical and compositional data

	2CCO	5CCO	10CCO
D_{Grain} [μm]	7.6 ± 1.0	2.3 ± 0.2	1.4 ± 0.3
d_{GB} [nm]	2.4 ± 0.5	1.7 ± 0.1	1.3 ± 0.3
E_a^{Grain} $T < 450\ °C$ [eV]	0.93 ± 0.01	0.88 ± 0.02	0.96 ± 0.01
E_a^{GB} [eV]	1.48 ± 0.13	1.06 ± 0.09	1.03 ± 0.08
$[Ca^{2+}]^{GB}$ [mol%]	18 ± 0.03	46 ± 0.05	40 ± 0.08

energy, thus decreasing the Arrhenius slope of σ_{Grain}.[31] While there is relatively little influence of nominal composition on E_a^{Grain}, E_a^{GB} decreases quickly with increasing Ca^{2+} content, in line with reported behavior of $Gd_xCe_{1-x}O_{2-x/2}$.[8] Here, the significant increase in σ_{GB} at low nominal solute concentration is attributed to reduced E_a^{GB}. Elucidating the origin of the large difference between σ_{GB} for 2CCO compared to 5CCO should illuminate design considerations for high-conductivity GBs.

The difference in σ_{GB} could result from differences in the GB character between the two materials.[16] Hence, EBSD (automated acquisition and indexing of back-scattered electron diffraction patterns) was employed to quantitatively compare the GB character of 2CCO and 5CCO.[32–34] Two-dimensional grain orientation datasets, *e.g.* Fig. 2a and c, were used to generate GB misorientation angle distributions (MADs, Fig. 2b and d) and grain boundary plane distributions (GBPDs, Fig. 2e and f) from >70 000 boundaries in each sample. The measured MADs, which describe the probability of observing various angles of misorientation between grains, were essentially identical for the two materials. Measured MADs exhibit only minor deviations from the so-called Mackenzie distribution, which is the analytically determined distribution for randomly oriented cubic crystals.[35,36] This indicated that 2CCO and 5CCO both exhibited randomly oriented grains without significant misorientation texture, consistent with microstructures observed in sintered yttria-zirconia.[37]

This result is corroborated by the GBPDs, which describe the relative area of different GB plane orientations. The GBPD is generated by normalizing the measured area of various GB plane orientations by that of a random, isotropic distribution. The GBPD is thus expressed in terms of multiples of the random distribution (MRD), with peaks of ±0.1 in the MRD not intense enough to be statistically significant, as is approximately the case here. For both 2CCO and 5CCO, the GBPDs are approximately unity, indicating that the two materials exhibit equivalently isotropic GB plane distributions. This result illustrates that from a microscopic viewpoint, the two samples' GB character is indistinguishable. Thus, the vast difference in σ_{GB} is not caused directly by changes in structural GB character.

To investigate local GB composition and chemistry, atomic-resolution annular dark field (ADF) imaging and nanoscale EELS measurements were performed using an AC-STEM. Ionic concentrations were measured using the $Ca\ L_{23}$, O K and $Ce\ M_{45}$ EELS ionization edges, and nanoscale chemistry was assessed *via* $Ce\ M_{45}$ near-edge fine structure. Inter-granular
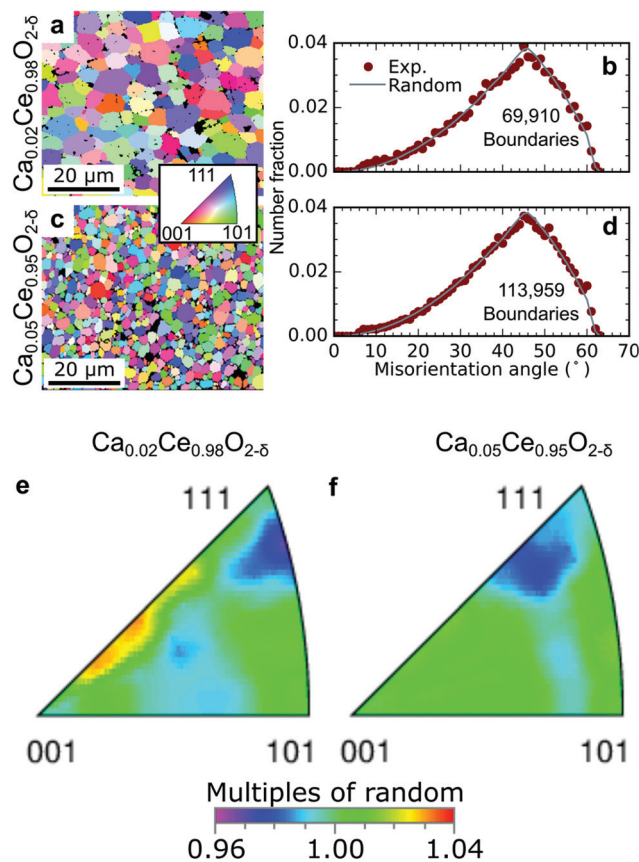

Fig. 2 (a, c) EBSD inverse pole figures of 2CCO and 5CCO indicating crystallographic directions of grains normal to the sample surface (according to the inset color-coded stereographic triangle). (b, d) MADs computed from experimental orientation data (Exp.) showing the number fraction of GBs of various misorientation angles, and the MAD for a randomly oriented cubic system. The number of GBs analyzed is provided. (e, f) GBPDs derived from stereological analysis of EBSD data, with MRD scale bar.

amorphous phases were not observed using phase contrast TEM imaging (see Fig. S3†), and no impurity phases were detected spectroscopically, which is consistent with XRD measurements and reasonable considering the high purity chemical precursors employed here.

Typical background-subtracted ionization edges are presented in Fig. 3a, showing the considerable differences in edge shape and intensity typically observed in grains (Off GB) and at GBs (On GB). In the GB vicinity, strong enhancement of the $Ca\ L_{23}$ edge intensity was accompanied by a decrease in the $Ce\ M_{45}$ signal, indicative of an enrichment of Ca^{2+} and depletion of Ce ions. Changes in the O K edge at GBs indicated considerable perturbation of the O bonding environment relative to grains.[23,24] Three main peaks in the O K edge (visible in the grain) are associated with O 1s core level excitations into unoccupied Ce levels,[38] and were typically not well resolved at GBs. Two of these peaks (5d e_g and 5d t_{2g}) arise from crystal-field splitting of the Ce–O bonding orbitals, hence smearing of the O K edge indicates the loss of long-range order due to altered anion coordination at the GB core.[23,39] This likely stems from

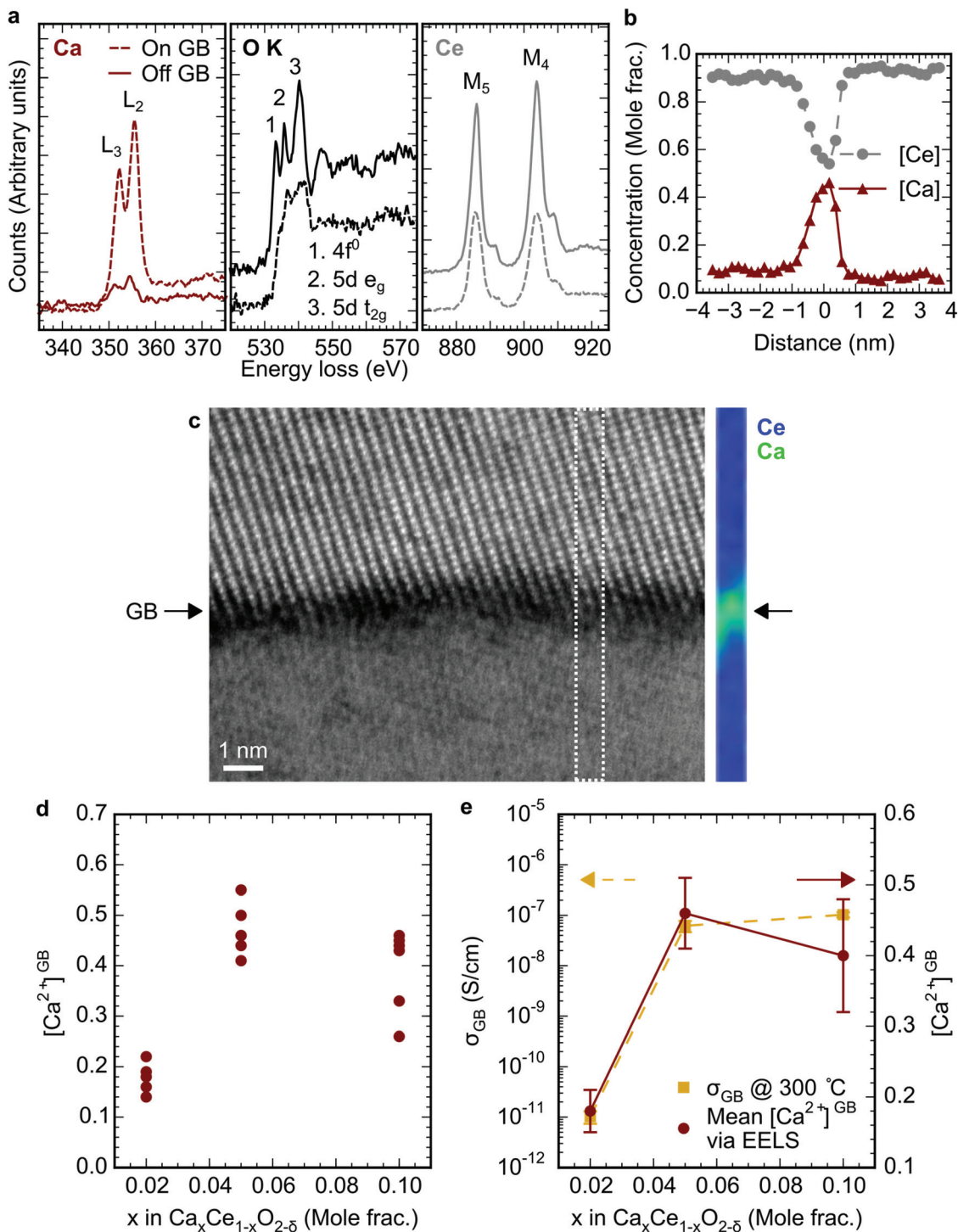Fig. 3 (a) Typical Ca L_{23}, O K and Ce M_{45} EELS edges from a GB (On GB) and a grain (Off GB, >5 nm from grain boundary) in 10CCO. Off GB O K and Ce M edges are shifted vertically for clarity. (b) Typical cation concentration profile in 10CCO, with GB centered at 0 nm. (c) ADF AC-STEM image of a grain boundary in 5CCO; the associated EELS elemental map (at right) was acquired in the region of (c) indicated with a dashed box (the probe step size was 2.5 Å, and the elemental map has been smoothed). (d) All EELS measurements of GB Ca^{2+} concentration, $[Ca^{2+}]^{GB}$. (e) Influence of nominal Ca^{2+} concentration, x, on σ_{GB} measured at 300 °C, and on $[Ca^{2+}]^{GB}$ (dashed and solid lines are guides for the eye).

combined effects of inherent oxygen deficiency which accommodates structural incoherence of the GB core,[40] and the presence of mobile O vacancies associated with segregated Ca^{2+} solutes.

Furthermore, reduction of the Ce $M_4 : M_5$ peak intensity ratio was observed at GBs, indicating the presence of Ce^{3+},[38,39] further suggesting O deficiency of the GB core.

Fig. 3c presents an AC-STEM ADF image from a GB where both grains, top and bottom, are oriented near a zone axis orientation. In this image, cation columns appear as bright spots, and lattice fringes from each grain are visible within Angstroms of the GB core, where there is a decrease in the ADF image intensity indicative of a decrease in high-angle scattering of incident electrons. As the ADF image contrast is sensitive to the atomic number of the scattering atom (there is so-called Z-contrast), this is in part the result of a greater concentration of Ca^{2+} cations, which are of lower atomic number than the Ce cations for which they substitute. This is corroborated by the Ce–Ca elemental map acquired from this boundary (right of ADF image), in which the Ca^{2+} concentration increases dramatically within 1–2 nm adjacent to the boundary, with the region of highest Ca^{2+} concentration coinciding with the GB core. We speculate that solute segregation in this case was driven by a combination of factors including (i) GB energy reduction, (ii) Coulomb interaction between the positive GB core charge and negatively-charged Ca^{2+} solutes (Ca''_{Ce}), and (iii) elastic strain due to ionic radius mismatch between Ca^{2+} solutes and host Ce ions ($Ce^{\times}_{Ce}$).[6]

These qualitative observations were substantiated by quantification of the GB Ca^{2+} concentration, $[Ca^{2+}]^{GB}$. Concentration profiles like that in Fig. 3b were measured in each sample, and used to determine mean $[Ca^{2+}]^{GB}$ (from profile maxima) and GB chemical width, d_{GB} (the width halfway between the grain and GB maximum concentrations). The mean d_{GB} was 1.8 ± 0.4 nm (calculated from the three d_{GB} values given in Table 1), and used to calculate σ_{GB} by eqn (2). All measured $[Ca^{2+}]^{GB}$ are shown in Fig. 3d, with the mean $[Ca^{2+}]^{GB}$ and standard deviation indicated in Fig. 3e (and Table 1). The mean $[Ca^{2+}]^{GB}$ in 2CCO is approximately 18 mol%, whereas $[Ca^{2+}]^{GB}$ in 5CCO and 10CCO is ca. 40 mol%–46 mol%. Based on the local GB Ca^{2+} concentration data presented in Fig. 3e, it is clear that the 5 mol% and 10 mol% samples have GB Ca^{2+} concentrations that are similar and substantially higher than the boundary concentration of the 2 mole% sample. Interestingly, XRD studies show that the lattice constant of CCO is proportional to the Ca^{2+} concentration below ~23 mol%,[30,41] suggesting that the super-saturated CCO observed here at GBs in 5CCO and 10CCO may not correspond to an equilibrium bulk phase, but rather a nanolayer GB complexion (a distinct GB phase) with thickness of one or two nanometers.[42] This complexion has a distinctly higher Ca^{2+} concentration than the GB complexion in 2CCO.

These data directly contradict the notion that GBs in conventionally sintered polycrystalline oxides are Mott–Schottky or Gouy–Chapman type interfaces, i.e. interfaces in a dilute solid solution. Indeed, this is not particularly surprising considering the foundational assumptions of both models: the Mott–Schottky model assumes a flat solute profile across the GB, and both models assume that point defect concentrations are sufficiently low such that defects can be treated as non-interacting. The defects can only be considered to be non-interacting for concentrations of approximately 1 mol%,[29] which is seldom the case in the literature on oxide ion-conducting solid

solutions. The acceptor cations are needed in relatively high concentration to yield a high concentration of mobile oxygen vacancies, so solute concentrations up to ~20 mol% are typically employed in common solid oxide electrolytes.[1,43]

A qualitative assessment of the spatial distributions of O at GB cores was determined via the anion-to-cation EELS signal intensity ratio, provided in Fig. S5,† which indicated O deficiency (i.e. oxygen vacancy enrichment) of the GB core. However, O vacancy depletion in the adjacent space charge zones could not be confirmed. (Similar oxygen profiles were reported for the yttria-stabilized zirconia system.[26]) Based on quantification of both $[Ca^{2+}]^{GB}$ and σ_{GB}, we thus speculate that a greater-than-expected concentration of O vacancies exists within the space charge zones, possibly due to accumulation of O vacancies associated with the high concentration of segregated Ca^{2+} cations.[29] The relatively strong defect association between Ca^{2+} and O vacancies—stemming from Coulomb attraction of the charged point defects, and the considerable cation size mismatch of Ca^{2+} (1.12 pm (ref. 44)) with Ce^{4+} (0.97 pm (ref. 44))[45,46]—may increase the propensity of O vacancies to accumulate with Ca^{2+} in the space charge zones. Thus, the higher concentration of O vacancies associated segregated Ca^{2+} may be a critical factor governing the enhanced σ_{GB}.

Fig. 3e compares the influence of nominal solute concentration on both σ_{GB} and $[Ca^{2+}]^{GB}$. In both cases, the effect of increasing the nominal Ca^{2+} content is minimal on σ_{GB} and $[Ca^{2+}]^{GB}$ for nominal concentrations above 5 mol%. This suggests that an upper limit to σ_{GB} may coincide with the nominal solute concentration corresponding to local boundary solute saturation. The trend shown in Fig. 3e along with the data in Table 1 suggests that σ_{GB} depends primarily on the GB composition. The direct observation of a correlation between the GB conductivity and high GB solute concentration is a seminal finding of this work, and represents a valuable insight for design and optimization of σ_{GB} in CCO and other oxide ionic conductors.

The notion that σ_{GB} is correlated with GB solute concentration, which can be several times greater than the nominal solute concentration,[11,23,47] may also be implied by prior reports. For instance, Avila-Paredes et al. showed that σ_{GB} in $Gd_xCe_{1−x}O_{2−\delta}$ is highly sensitive to nominal Gd^{3+} concentration below ca. 6 mol%, before gradually plateauing around 15 mol% Gd^{3+}.[8] Based on the present study, one could attribute this high sensitivity at low nominal Gd^{3+} concentration and subsequent plateau of σ_{GB} to nanoscale GB saturation of Gd^{3+}.[11,23] Furthermore, there is utility in knowledge of the optimal GB solute concentration for maximizing σ_{GB}: when synthesis conditions do not favor strong solute segregation, such as intermediate temperature thin film deposition using pulsed laser deposition,[4,12,14] knowledge of the desired GB solute concentration could guide post-deposition processing.[14] Shirpour et al.[9] proposed GB core decoration to increase σ_{GB} by mitigating deleterious space-charge effects in proton conducting barium zirconate-based solid solutions. This is consistent with experimental evidence presented here, and has generally been corroborated in other oxide conducting

materials.[13,14,17,18] However, unlike previous works, the present study demonstrates explicitly the correlation between high local GB solute concentration and σ_{GB} in an oxide ion conductor.

Models describing the electrical properties of GBs characterized in this work must account for high GB solute concentrations and treat point defect interactions. A potentially suitable model to describe the GBs presented here is the recently developed Hilliard–Cahn model proposed by Mebane and De Souza.[29] This model was successfully employed to reproduce experimentally-measured σ_{GB} in $Gd_xCe_{1-x}O_{2-\delta}$ (0.01 < x < 0.2). The predicted trend in the GB Gd^{3+} solute content with nominal solute concentration agrees qualitatively with the experimental trend observed here for Ca^{2+} solutes. Indeed, the trends observed here may be applicable to other polycrystalline solid solution electrolytes whose σ_{GB} is governed or influenced by space charge effects, such as proton-conducting barium zirconates and cerates, lithium-conducting oxides like lithium lanthanum zirconate, and oxide conducting fluorites and perovskites such as zirconia, ceria and strontium titanate.

In summary, we have demonstrated correlation between macroscopic σ_{GB} and high GB Ca^{2+} concentration in CCO using a combination of AC impedance spectroscopy and AC-STEM EELS. The roles of structural GB character—measured using EBSD—and local GB solute concentration on σ_{GB} were assessed independently, and it was concluded that σ_{GB} is primarily regulated by changes in the local solute concentration, rather than differences in microscopic GB character. Specifically, increasing the nanoscale Ca^{2+} concentration at the GB from 18 mol% to 46 mol% results in a four-order-of-magnitude increase in σ_{GB} and at least a two order of magnitude increase in total conductivity. This confirms our hypothesis that σGB is primarily controlled by local GB composition rather than GB character. Because solute segregation is thermodynamically driven, the behavior observed in this system should be generally applicable to other polycrystalline electroceramics. This fundamental understanding will guide design and fabrication of electroceramic grain boundaries with optimized transport properties. The local GB cation concentration far exceeds the range of validity for application of traditional Mott Schottky and Gouy–Chapman models. High solute concentrations are likely present in many technologically relevant electroceramics, which highlights the need to develop new models to explain GB conductivity over a wide range of GB compositions.

Experimental

Material fabrication

Nanoparticles were spray dried from >99.999% pure hydrated-nitrate salt precursors, before being calcined, compacted, and sintered to pellets (18 mm diameter discs, 1 mm thick) at 1400 °C for 24 h (see also Fig. S1†).[11]

AC impedance spectroscopy

The parallel pellet faces were polished using 1 μm lapping film before porous Pt ink electrodes were applied.[11] Samples were heated stepwise in air between 150 °C and 700 °C, and impedance measurements were performed using a Gamry Reference 3000 potentiostat with applied voltage of 50 mV over the frequency range 1 MHz to 0.1 Hz. Data were fit to the equivalent circuit model inset in Fig. 1d using the Gamry E-Chem Analyst software.

Electron backscatter diffraction (EBSD)

Parallel pellet faces were polished using a series of diamond suspensions ranging from 9 μm to 0.05 μm. To reduce charging effects, conductive Ag paint was applied near regions of interest, and to mount samples on the sample holder (PELCO®, Ted Pella, Inc.). An FEI Quanta 200 SEM with EDAX OIM EBSD software, and an FEI Quanta 600 SEM with Oxford Instrument's AZtec EBSD software were used to collect grain orientation data. SEM imaging was performed with 10 mm working distance and 15 kV accelerating voltage. EBSD patterns were acquired with 70° sample tilt, 4 × 4 binning, 100 frames per s acquisition rate, and variable gain. Post processing was performed using TSL software, and included cleaning using grain dilation with a minimum grain size of 5 pixels per grain and grain tolerance angle of 5°, single average orientation per grain, grain confidence index (CI) standardization and partition of 0.1 CI to remove poorly indexed points. After cleanup, reconstructed boundaries were extracted as grain boundary line segments. Grain boundary character distributions were calculated, independent of misorientation, using five parameter stereological analysis.[48]

Scanning transmission electron microscopy (STEM)

Specimens were prepared by mechanical dimpling followed by Ar^+ ion milling (Gatan PIPS2 mill): 5 keV accelerating voltage to puncture the dimpled foil, and 1 keV final thinning. A JEOL ARM 200F AC-STEM Gatan Enfina EELS was employed with 20 mrad convergence and 42 mrad collection semi-angles. Only GBs oriented approximately parallel to the electron beam were selected for EELS analysis. This was accessed by the apparent GB width visible during ADF imaging. Spectral processing and smoothing of the elemental map in Fig. 3 was performed using Gatan DigitalMicrograph software, and involved subtraction of the extrapolated inverse power law function fit to the pre-edge intensity.[49] Background fitting and signal integration windows are provided in Table S2;† integration windows greater than 50 eV were employed to minimize processing artifacts related to plural scattering. Spectra were calibrated assuming the Ce M_5 edge maximum is located at 883 eV. Elemental concentrations (C_i) were estimated from background-subtracted signal intensities (I_i) using

$$C_A/C_B = (I_A/I_B) \cdot k_{AB} \tag{4}$$

where k_{AB} is the ratio of scattering cross-sections of elements A and B.[49] This so-called k-factor was measured in 10CCO grains, where the nominal composition was assumed, and was

taken to be constant in grains and at grain boundaries. Background fitting and signal integration windows, along with k-factors are provided in Table S2.† The derived composition on either side of GBs was very similar, suggesting that channeling effects do not significantly influence the quantification in this case.

Data processing

The Python Pyzo integrated development environment (v.2015a, open source) was employed for further data processing, and figures were prepared using the Inkscape graphics editor (v.0.91, open source).

Author contributions

C. A. H. prepared the CCO starting material, fabricated pellets, and performed SEM imaging and XRD measurements. M. N. K. performed EBSD data acquisition and analysis. M. N. K. and G. S. R. were responsible for the final interpretation of EBSD data. W. J. B. performed impedance spectroscopy and TEM data acquisition and analysis. W. J. B. and P. A. C. were responsible for the final interpretation of electrical and TEM data. W. J. B. prepared the figures and manuscript with input from C. A. H., M. N. K., G. S. R. and P. A. C. G. S. R. and P. A. C. co-supervised the study.

Funding sources

Conflicts of interest

There are no conflicts to declare.

Acknowledgements

References

1 E. D. Wachsman and K. T. Lee, Lowering the Temperature of Solid Oxide Fuel Cells, *Science*, 2011, **334**, 935–939.

2 J. Sunarso, S. Baumann, J. M. Serra, W. A. Meulenberg, S. Liu, Y. S. Lin, *et al.*, Mixed ionic–electronic conducting (MIEC) ceramic-based membranes for oxygen separation, *J. Membr. Sci.*, 2008, **320**(1–2), 13–41.

3 S. M. Haile, D. L. West and J. Campbell, The role of microstructure and processing on the proton conducting properties of gadolinium-doped barium cerate, *J. Mater. Res.*, 1998, **13**(6), 1576–1595.

4 S. Schweiger, R. Pfenninger, W. J. Bowman, U. Aschauer and J. L. M. Rupp, Designing Strained Interface Heterostructures for Memristive Devices, *Adv. Mater.*, 2017, 1605049–1605011.

5 X. Guo, W. Sigle and J. Maier, Blocking Grain Boundaries in Yttria-Doped and Undoped Ceria Ceramics of High Purity, *J. Am. Ceram. Soc.*, 2003, **86**(1), 77–87.

6 X. Guo and R. Waser, Electrical properties of the grain boundaries of oxygen ion conductors: Acceptor-doped zirconia and ceria, *Prog. Mater. Sci.*, 2006, **51**, 151–210.

7 A. Jasper, J. A. Kilner and D. W. McComb, TEM and impedance spectroscopy of doped ceria electrolytes, *Solid State Ionics*, 2008, **179**(21–26), 904–908.

8 H. J. Avila-Paredes, K. Choi, C.-T. Chen and S. Kim, Dopant-concentration dependence of grain-boundary conductivity in ceria: A space-charge analysis, *J. Mater. Chem.*, 2009, **19**(27), 4837.

9 M. Shirpour, B. Rahmati, W. Sigle, P. A. van Aken, R. Merkle and J. Maier, Dopant Segregation and Space Charge Effects in Proton-Conducting $BaZrO_3$ Perovskites, *J. Phys. Chem. C*, 2012, **116**(3), 2453–2461.

10 C. Ma, K. Chen, C. Liang, C.-W. Nan, R. Ishikawa, K. More, *et al.*, Atomic-scale origin of the large grain-boundary resistance in perovskite Li-ion-conducting solid electrolytes, *Energy Environ. Sci.*, 2014, **7**(5), 1638.

11 W. J. Bowman, J. Zhu, R. Sharma and P. A. Crozier, Electrical conductivity and grain boundary composition of Gd-doped and Gd/Pr co-doped ceria, *Solid State Ionics*, 2015, **272**, 9–17.

12 J. Sheth, D. Chen, J. J. Kim, W. J. Bowman, P. A. Crozier, H. L. Tuller, *et al.*, Coupling of strain, stress, and oxygen non-stoichiometry in thin film $Pr_{0.1}Ce_{0.9}O_{2-\delta}$, *Nanoscale*, 2016, **8**(36), 16499–16510.

13 E. M. Mills, M. Kleine-Boymann, J. Janek, H. Yang, N. D. Browning, Y. Takamura, *et al.*, YSZ thin films with minimized grain boundary resistivity, *Phys. Chem. Chem. Phys.*, 2016, **18**(15), 10486–10491.

14 S. J. Litzelman, R. A. De Souza, B. Butz, H. L. Tuller, M. Martin and D. Gerthsen, Heterogeneously doped nanocrystalline ceria films by grain boundary diffusion: Impact on transport properties, *J. Electroceram.*, 2009, **22**(4), 405–415.

15 A. Tschöpe, S. Kilassonia and R. Birringer, The grain boundary effect in heavily doped cerium oxide, *Solid State Ionics*, 2004, **173**(1–4), 57–61.

16 F. Ye, C. Y. Yin, D. R. Ou and T. Mori, Relationship between lattice mismatch and ionic conduction of grain boundary in YSZ, *Prog. Nat. Sci.: Mater. Int.*, 2014, **24**(1), 83–86.

17 D. R. Diercks, J. Tong, H. Zhu, R. Kee, G. Baure, J. C. Nino, *et al.*, Three-dimensional quantification of composition and electrostatic potential at individual grain boundaries in doped ceria, *J. Mater. Chem. A*, 2016, **4**(14), 5167–5175.

18 H. J. Avila-Paredes and S. Kim, The effect of segregated transition metal ions on the grain boundary resistivity of gadolinium doped ceria: Alteration of the space charge potential, *Solid State Ionics*, 2006, **177**(35–36), 3075–3080.

19 Y. Lin, S. Fang, D. Su, K. S. Brinkman and F. Chen, Enhancing grain boundary ionic conductivity in mixed ionic–electronic conductors, *Nat. Commun.*, 2015, **6**, 6824.

20 H. L. Tuller and S. R. Bishop, Point Defects in Oxides: Tailoring Materials Through Defect Engineering, *Annu. Rev. Mater. Res.*, 2011, **41**(1), 369–398.

21 S. Kim, Isn't the space-charge potential in ceria-based solid electrolytes largely overestimated?, *Phys. Chem. Chem. Phys.*, 2016, **18**(29), 19787–19791.

22 S. Kim, S. K. Kim, S. Khodorov, J. Maier and I. Lubomirsky, On determining the height of the potential barrier at grain boundaries in ion-conducting oxides, *Phys. Chem. Chem. Phys.*, 2016, **18**(4), 3023–3031.

23 Y. Lei, Y. Ito, N. D. Browning and T. J. Mazanec, Segregation Effects at Grain Boundaries in Fluorite-Structured Ceramics, *J. Am. Ceram. Soc.*, 2002, **85**(9), 2359–2363.

24 N. D. Browning, R. F. Klie and Y. Lei, Vacancy Segregation at Grain Boundaries in Ceramic Oxides, in *Mixed Ionic Electronic Conducting Perovskites for Advanced Energy Systems*, Kluwer, The Netherlands, 2004. pp. 15–25.

25 W. Lee, H. J. Jung, M. H. Lee, Y.-B. Kim, J. S. Park, R. Sinclair, *et al.*, Oxygen Surface Exchange at Grain Boundaries of Oxide Ion Conductors, *Adv. Funct. Mater.*, 2012, **22**(5), 965–971.

26 J. An, J. S. Park, A. L. Koh, H. B. Lee, H. J. Jung, J. Schoonman, *et al.*, Atomic Scale Verification of Oxide-Ion Vacancy Distribution near a Single Grain Boundary in YSZ, *Sci. Rep.*, 2013, **3**, 2680–2686.

27 N. Nafsin, J. A. Aguiar, T. Aoki, A. M. Thron, K. van Benthem and R. H. R. Castro, Thermodynamics versus kinetics of grain growth control in nanocrystalline zirconia, *Acta Mater.*, 2017, **136**, 224–234.

28 H. B. Lee, F. B. Prinz and W. Cai, Atomistic simulations of grain boundary segregation in nanocrystalline yttria-stabilized zirconia and gadolinia-doped ceria solid oxide electrolytes, *Acta Mater.*, 2013, **61**(10), 3872–3887.

29 D. S. Mebane and R. A. De Souza, A generalised space-charge theory for extended defects in oxygen-ion conducting electrolytes: from dilute to concentrated solid solutions, *Energy Environ. Sci.*, 2015, **8**(10), 2935–2940.

30 H. Arai, T. Kunisaki, Y. Shimizu and T. Seiyama, Electrical Properties of Calcia-Doped Ceria with Oxygen Ion Conduction, *Solid State Ionics*, 1986, **20**, 241–248.

31 J. A. Kilner and C. D. Waters, The effects of dopant cation-oxygen vacancy complexes on the anion transport properties of non-stoichiometric fluorite oxides, *Solid State Ionics*, 1982, **6**(3), 253–259.

32 G. S. Rohrer, D. M. Saylor, B. E. Dasher, B. L. Adams, A. D. Rollett and P. Wynblatt, The distribution of internal interfaces in polycrystals, *Z. Metallkd.*, 2004, **95**(4), 197–214.

33 G. S. Rohrer, Measuring and Interpreting the Structure of Grain-Boundary Networks: Measuring and Interpreting the Structure of Grain-Boundary Networks, *J. Am. Ceram. Soc.*, 2011, **94**(3), 633–646.

34 M. N. Kelly, K. Glowinski, N. T. Nuhfer and G. S. Rohrer, The five parameter grain boundary character distribution of α-Ti determined from three-dimensional orientation data, *Acta Mater.*, 2016, **111**, 22–30.

35 J. K. Mackenzie, Second Paper on Statistics Associated with the Random Disorientation of Cubes, *Biometrika*, 1958, **45**(1/2), 229.

36 J. K. Mason and C. A. Schuh, The generalized Mackenzie distribution: Disorientation angle distributions for arbitrary textures, *Acta Mater.*, 2009, **57**(14), 4186–4197.

37 L. Helmick, S. J. Dillon, K. Gerdes, R. Gemmen, G. S. Rohrer, S. Seetharaman, *et al.*, Crystallographic Characteristics of Grain Boundaries in Dense Yttria-Stabilized Zirconia, *Int. J. Appl. Ceram. Technol.*, 2011, **8**(5), 1218–1228.

38 D. R. Mullins, S. H. Overbury and D. R. Huntley, Electron spectroscopy of single crystal and polycrystalline cerium oxide surfaces, *Surf. Sci.*, 1998, **409**, 307–319.

39 H. Hojo, T. Mizoguchi, H. Ohta, S. D. Findlay, N. Shibata, T. Yamamoto, *et al.*, Atomic Structure of a CeO_2 Grain Boundary: The Role of Oxygen Vacancies, *Nano Lett.*, 2010, **10**(11), 4668–4672.

40 S. Kim, P. Jain, H. J. Avila-Paredes, A. Thron, K. van Benthem and S. Sen, Strong immobilization of charge carriers near the surface of a solid oxide electrolyte, *J. Mater. Chem.*, 2010, **20**(19), 3855.

41 K. Eguchi, T. Kunisaki and H. Arai, Effect of Microstructures on the Ionic Conductivity of Ceria-Calcia Oxides, *J. Am. Ceram. Soc.*, 1986, **69**(11), c282–c285.

42 P. R. Cantwell, M. Tang, S. J. Dillon, J. Luo, G. S. Rohrer and M. P. Harmer, Grain boundary complexions, *Acta Mater.*, 2014, **62**, 1–48.

43 M. Mogensen, N. M. Sammes and G. A. Tompsett, Physical, chemical and electrochemical properties of pure and doped ceria, *Solid State Ionics*, 2000, **129**(1–4), 63–94.

44 R. D. Shannon, Revised effective ionic radii and systematic studies of interatomic distances in halides and chalcogenides, *Acta Crystallogr., Sect. A: Cryst. Phys., Diffr., Theor. Gen. Cryst.*, 1976, **32**(5), 751–767.

45 K. Eguchi, T. Setoguchi, T. Inoue and H. Arai, Electrical properties of ceria-based oxides and their application to solid oxide fuel cells, *Solid State Ionics*, 1992, **52**(1–3), 165–172.

46 J. L. M. Rupp, E. Fabbri, D. Marrocchelli, J.-W. Han, D. Chen, E. Traversa, *et al.*, Scalable Oxygen-Ion Transport Kinetics in Metal-Oxide Films: Impact of Thermally Induced Lattice Compaction in Acceptor Doped Ceria Films, *Adv. Funct. Mater.*, 2014, **24**(11), 1562–1574.

47 S. Taub, R. E. A. Williams, X. Wang, D. W. McComb, J. A. Kilner and A. Atkinson, The effects of transition metal oxide doping on the sintering of cerium gadolinium oxide, *Acta Mater.*, 2014, **81**, 128–140.

48 D. M. Saylor and G. S. Rohrer, Determining Crystal Habits from Observations of Planar Sections, *J. Am. Ceram. Soc.*, 2002, **85**(11), 2799–2804.

49 R. F. Egerton, *Electron Energy-Loss Spectroscopy in the Electron Microscope*, Springer, New York, 3rd edn, 2011.

50 C. H. Shen, R. S. Liu, J. G. Lin and C. Y. Huang, Phase stability study of $La_{1.2}Ca_{1.8}Mn_2O_7$, *Mater. Res. Bull.*, 2001, **36**(5), 1139–1148.

51 V. Kotov and S. Reichstein, *Zh. Fiz. Khim.*, 1941, **15**, 1057–1058.